Faculty and Researchers   Faculty and Researchers' Publications

2019

The effect of interface shock viscosity on the strain rate induced temperature rise in an energetic material analyzed using the cohesive finite element method

Prakash, Chandra; Gunduz, I. Emre; Tomar, Vikas

IOP Publishing

The effect of interface shock viscosity on the strain rate induced temperature rise in an energetic material analyzed using the cohesive finite element method

Chandra Prakash[1] , I Emre Gunduz[2,3] and Vikas Tomar[1]

[1] School of Aeronautics and Astronautics, Purdue University, IN 47907, United States of America
[2] School of Mechanical Engineering, Purdue University, IN 47907, United States of America
[3] Mechanical and Aerospace Engineering Department, Naval Postgraduate School, Monterey, CA, United States of America

E-mail: tomar@purdue.edu

CrossMark

Abstract

In this work, shock induced failure and local temperature rise behavior of a hydroxyl-terminated polybutadiene (HTPB)—ammonium perchlorate (AP) energetic material is modeled using the cohesive finite element method (CFEM). Thermomechanical properties used in the model were obtained from four different experiments: (1) dynamic impact experimental measurements for fitting a viscoplastic constitutive model, (2) *in situ* mechanical Raman spectroscopy (MRS) measurements of the separation properties for fitting a cohesive zone model, (3) a pulse laser induced particle impact experiment combined with the MRS for measurement of the interface shock viscosity, and (4) Raman thermometry experiments for measurement of HTPB, AP, and HTPB-AP interface thermal conductivity. HTPB-AP interface regions with high density of particles were found to be more susceptible to local temperature rise due to the presence of viscoplastic dissipation as well as frictional heating. The increase in the interface shock viscosity lead to a decrease in both the viscoplastic and frictional dissipation. This resulted in a decrease in the maximum temperature and the density of local regions with a maximum temperature rise within the HTPB-AP microstructure. A power law relation for the decrease in viscoplastic energy dissipation, temperature rise and the density of the local temperature rise with the interface shock viscosity was obtained.

1. Introduction

Energetic materials are composites which consists of an oxidizer material embedded in a polymer binder. A mixture of hydroxyl-terminated polybutadiene (HTPB) and ammonium perchlorate (AP) is one example that is mostly used in solid rocket propellant [1]. These materials are susceptible to failure due to external impact or temperature change and thus, initiation and subsequent detonation can occur at unintended times. Energetic materials are known to initiate at regions of sufficient size and temperature that could cause detonation [2]. One key factor that may result in this type of mechanical and thermal behavior of is the heterogeneous nature of energetic material microstructure. In order to determine causes and possible prevention mechanisms, a proper understanding of the underlying mechanisms involved in hot-spot formation under high strain rate impact is necessary.

Several researchers have attempted to identify the critical size, temperature, and time span of hot spots necessary to cause initiation of detonation, which in many cases are found to occur due to cracks, voids or other mechanisms, [1, 3]. There have been attempts to identify different mechanisms for hot spot formation in microstructure, such as, the adiabatic compression of trapped gases, heating at crack tips, viscous heating of material between impacting surfaces, friction between sliding or impacting surfaces, and friction during mechanical failure [1]. Temperature increase due to frictional energy dissipation within the microstructure at contact between failed surfaces is an important consideration. A few of the several reasons of microstructural failure in energetic materials have been found to be; particle failure, particle-binder debonding, and cavitation and pore collapse [4]. However any combination of the three can be found to occur simultaneously. Among the above listed failure mechanisms, the most dominant failure has been found to be the particle-binder interface debonding [5] for hot spot formation as cracks have been found to propagate mostly along such interfaces [6]. Subsequent studies have shown that the fracture resistance of these materials is highly dependent on the strength of the interfaces [7]. This strength, in turn, has been found to be dependent on the material constituents and their relative sizing. Drodge *et al* [8], studied the effect of particle size on the mechanical behavior of energetic materials, which showed a decrease in yield strain caused by an increase in particle size. Experimental observations, by Rae *et al* [6], also showed that the failures starts around larger particles with cracks preferentially propagating along interfaces.

A physical property that has been critical in predicting the influence of mechanical loading on the temperature rise in the energetic material microstructures is the shock viscosity [2]. Solids, under a sufficiently high pressure and high strain rate, deform in a manner similar to fluids, which is considered to be a result of the concomitant motion of defects [9]. In the shock regime, the dissipative processes within the microstructure are governed by plastic deformation and damage as well as material viscosity, called shock viscosity [10, 11]. The shock viscosity is responsible for the energy dissipation that accompanies the local rate of shear deformation and affects the temperature increase in the material undergoing shock loading. Benson *et al* [2] have shown that the temperature increase due to impact is higher in the inviscid case than when the shock viscosity is taken into account. Many researchers have used experimental techniques such as VISAR, [12–15], for the shock wave rise time measurements in order to determine shock viscosity. Kanel *et al* [13], have observed that the

shock viscosity is significantly affected by applied strain rate. Several researchers [13, 16, 17] have shown the dependence of the exponent in the power law relation between strain rate and shock stress on material properties, such as density, viscosity etc, as well as microstructural parameters such as porosity, particle size [16], the material heterogeneity [18] and the interface impedance mismatch [19]. Recently Prakash *et al* [20], have used a novel experimental approach based on particle impact and MRS to measure the interface shock viscosity for an HTPB-AP material interface and showed that the value of interface shock viscosity changes with the interface chemical composition.

In this work, the mechanical response of an HTPB-AP energetic material microstructure under shock loading for different interface chemical compositions of HTPB-AP interfaces is modeled using the cohesive finite element method (CFEM). The chemical composition of the HTPB-AP interface is altered by adding binding agents which has been shown to change the mechanical properties, such as stiffness, failure strength [21], as well as the interface viscosity [20]. CFEM is based on the cohesive zone approach which uses a micro-scale level local failure behavior based damage model. This technique can be implemented to model fracture in individual components as well as the interface separation behavior of the microstructure. Cohesive zone models (CZMs) have been used by many researchers [22–25] to simulate the interface debonding. Barua *et al* [22, 23, 26, 27] have studied the microstructural level response of various idealized PBXs under shock induced impact loading using CZM. However the numerical models used in the literature [28–31], do not include shock viscosity, especially the interface shock viscosity, as well as the strain rate dependent interface constitutive model.

For the purposes of this work, cohesive parameters are obtained experimentally through *in situ* mechanical Raman spectroscopy (MRS) measurements [21, 32, 33]. As high strain rates are used, the material is modeled using viscoplastic constitutive behavior [20, 21, 33]. The remaining part of the paper is arranged as follows: section 2 the CFEM method and constitutive models used to simulate the impact behavior of the HTPB-AP samples. Section 3 briefly describes the sample preparation and experimental procedures for measuring the material mechanical properties based on work in [21]. Section 4 presents the results obtained from experimental measurement of thermal conductivity along with the numerical simulation of the impact of EM composites. Section 5 presents the summary and conclusions.

2. CFEM framework

CFEM has been used extensively for simulating the impact induced damage behavior of different composite materials [34–40], including energetic materials [22–24, 41]. CFEM application to a material with unknown crack path can be approached in two ways; the first is to dynamically insert cohesive surfaces into the model as fracture develops and the second is to define all bulk element boundaries as cohesive surfaces. For the purposes of this work, the second approach is employed [20, 21, 42]. The finite element mesh for the modeled microstructure was generated with 'cross triangle' elements and cohesive surfaces at all element boundaries, as shown in figure 1. The rectangular mesh size for all of the models, which contains four 'cross triangle' elements each, was 1 μm, creating 250 000 elements in the domain. The mesh size was chosen based on the criterion outlined by Tomar *et al* [43]. The 1 μm thick interface was modeled with a 0.5 μm thick bulk element.
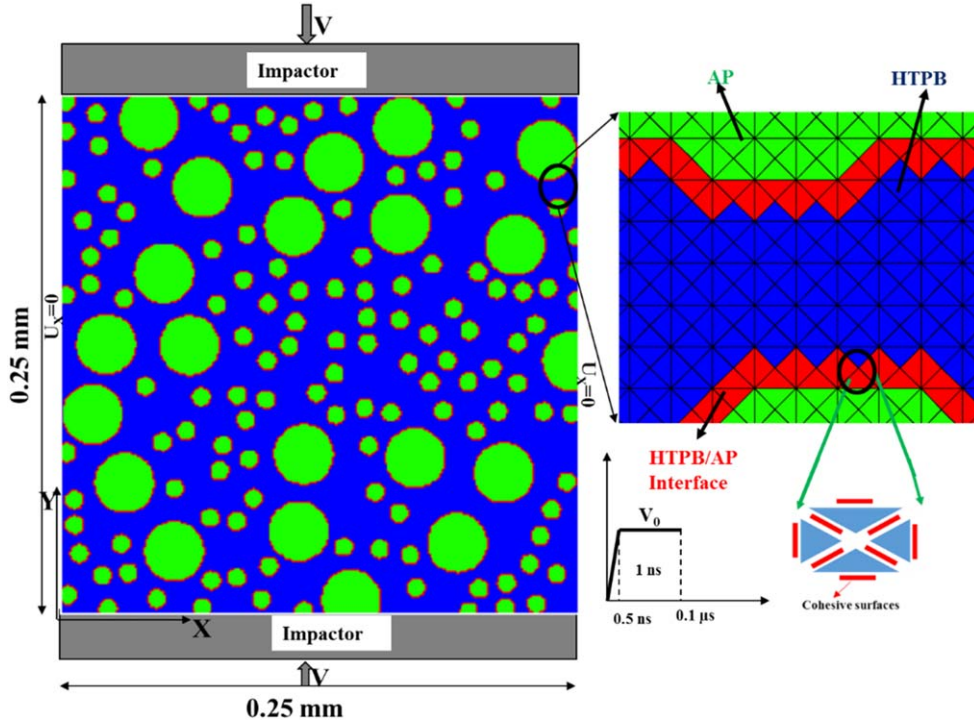
Figure 1. The finite element model of HTPB-AP microstructure (50% AP density) showing boundary conditions, and the mesh details as well as cohesive surfaces.

The weak form of the cohesive finite element model is given by

$$\int_V \boldsymbol{\tau}: \delta \boldsymbol{F} \, dV - \int_{S_{\text{int}}} \boldsymbol{T} \cdot \delta \Delta \, dS = \int_{S_{\text{ext}}} \boldsymbol{T} \cdot \delta \boldsymbol{u} \, dS - \int_V \rho \frac{\partial^2 \boldsymbol{u}}{\partial t^2} \cdot \delta \boldsymbol{u} \, dV. \tag{1}$$

Here, $\boldsymbol{\tau}$ is the Kirchhoff's stress, $\boldsymbol{F}$ is the deformation gradient, $\boldsymbol{u}$ is the displacement, t is the time, V is the volume, S is the surface area, $\boldsymbol{T}$ is the applied traction and Δ is the surface separation, in the reference configuration, on material point on a cohesive surface.

For the continuum elements, a viscoplastic constitutive model is used to govern the stress-strain relations while the irreversible bilinear cohesive law for tensile separation is used to govern the separation at the cohesive surfaces. The large deformation viscoplastic model has been described in an earlier work by the authors [20]. The velocity gradient tensor $\boldsymbol{L}$ is decomposed into a rate of deformation, $\boldsymbol{D}$, and the spin tensor, $\boldsymbol{W}$, as

$$\boldsymbol{L} = \dot{\boldsymbol{F}} \cdot \boldsymbol{F}^{-1} = \boldsymbol{D} + \boldsymbol{W} = (\boldsymbol{D}^e + \boldsymbol{D}^{vp}) + (\boldsymbol{W}^e + \boldsymbol{W}^{vp}), \tag{2}$$

The Jaumann objective rate is used in the model and the rate of deviatoric part of Kirchhoff's stress is given as

$$\hat{\boldsymbol{\tau}}' = \boldsymbol{\tau}' - \boldsymbol{W} \cdot \boldsymbol{\tau}' + \boldsymbol{\tau}' \cdot \boldsymbol{W} = \boldsymbol{C}: [\boldsymbol{D}' - \boldsymbol{D}^{vp'}]. \tag{3}$$

where $\boldsymbol{C}$ is the elastic stiffness tensor. The constitutive laws for the viscoplastic part of both $\boldsymbol{D}^{vp}$ and $\boldsymbol{W}^{vp}$ are required for a finite plastic deformations [44]. Here, it is assumed that the material is in a relaxed configuration which is not spinning, i.e. the viscoplastic spin rate $\boldsymbol{W}^{vp} = 0$, [45]. The flow rule for large deformation for an isotropic hardening solid, $\boldsymbol{D}^{vp}$, is given by

Table 1. Mie–Gruneisen parameters for HTPB and AP [47].

	K (10^5 MPa)	A (10^5 MPa)	B (10^5 MPa)	γ	ρ_0 g cm^{-3}	E (MPa)	ν
HTPB	0.02	0.294	0.0196	0.7	0.9	2.5	0.45
AP	0.15	0.225	0.1863	1.0	1.95	20000	0.23

$$D_{ij}^{vp} = \frac{\partial f}{\partial \tau_{ij}} \dot{\lambda} = \frac{3}{2\overline{\sigma}} \tau'_{ij} \dot{\lambda}, \tag{4}$$

where f is defined as the Mises yield function [46], and $\dot{\lambda}$ is equal to an effective viscoplastic strain rate, given by

$$\dot{\lambda} = \sqrt{\frac{2}{3} D_{ij}^{vp} D_{ij}^{vp}} = \dot{\overline{\varepsilon}}^{vp} = \frac{d\overline{\varepsilon}^{vp}}{d\overline{\sigma}} \dot{\overline{\sigma}}, \tag{5}$$

$$\overline{\sigma} = \sqrt{\frac{3}{2} \tau'_{ij} \tau'_{ij}}, \tag{6}$$

and $\overline{\varepsilon}^{vp}$ is the effective viscoplastic strain obtained from a nanoscale dynamic impact experiment explained in section 3. A modified Kirchoff stress is used to include viscous stress, and is given by

$$\boldsymbol{\tau} = \boldsymbol{\tau}' + \boldsymbol{\tau}^v - pI, \tag{7}$$

where $\tau_{ij}^v = \eta D_{ij}$ [2] and the pressure is calculated from a polynomial form of the Mie–Gruneisen equation of state as

$$p = K\phi + A\phi^2 + B\phi^3 + \gamma(1 + \varphi)e \tag{8}$$

where

$$\phi = \frac{\rho}{\rho_0} - 1 = \frac{1}{J} - 1 = \frac{1}{\det(\boldsymbol{F})} - 1.$$

e is the internal energy per unit volume, γ is the Gruneisen parameter, K is the Bulk Modulus and, A, and B are parameters obtained from [47] and are given in table 1 for HTPB and AP. Here ρ_0 is the initial density, E is the Young's modulus and ν is the Poisson ratio.

In this work we have used an irreversible bilinear CZM [43]. In order to obtain the cohesive zone parameters for AP-HTPB interfaces, delamination experiments at AP-HTPB interfaces in the analyzed samples are performed and the local stress is measured using an *in situ* MRS as explained in section 3. In order to prevent the interpenetration of bulk elements, an acceleration correction term is used that is obtained based on a frictional cohesive contact model developed by Baek *et al* [48] for large deformation impact simulation. As was shown in a previous work by the authors [20], the element penetration in this model is insignificant for the total time of the simulation.

In order to identify the local temperature rise within the microstructure, a threshold temperature increase from the reference temperature was chosen. Temperature increase, $\Delta T = T - T_{\mathrm{ref}}$, was calculated from [2]

$$T = \frac{e + e_f - e_c}{\rho c_p}, \tag{9}$$

where, $T_{\mathrm{ref}} = 298$ K, e is the internal energy density of the system, e_f is the frictional dissipation energy density, e_c is the cold compression energy density, ρ is the material density

and c_p is the heat capacity at constant pressure. The cold compression energy density, e_c is given as [2]

$$e_c = \int_1^\phi \frac{p}{\varphi^2} d\varphi - \rho c_p T_{\text{ref}} e^{[a(1-1/\phi)]\phi^{1-a}}$$
$$\phi = \rho/\rho_0 = 1/J = 1/\det(\boldsymbol{F}), \tag{10}$$

where $\boldsymbol{F}$ is the deformation gradient, p is the pressure and a is the first order volume correction factor for γ. In this work, the value of a is taken to be equal to zero for all of the materials [2]. The rate of heat generation (h) by the frictional forces at the bulk element interfaces were obtained from [34],

$$h = \boldsymbol{T} \cdot [\![v]\!], \tag{11}$$

where $\boldsymbol{T}$ is the contact traction acting at the interface and $[\![v]\!]$ is the jump in velocity of the surfaces in contact. This frictional heat (h) is then distributed among the contacting bulk elements (element 1 and element 2) based on ratio of heat supply given by Camacho and Ortiz [34] as

$$\frac{\dot{e}_f^1}{\dot{e}_f^2} = \frac{\sqrt{\kappa_1 \rho_1 c_1}}{\sqrt{\kappa_2 \rho_2 c_2}},$$
$$h = \dot{e}_f^1 + \dot{e}_f^2, \tag{12}$$

where κ is the thermal conductivity and c is the specific heat at constant pressure of the bulk element involving the interface. The thermal conductivity for the HTPB-AP interface was obtained using Raman thermometry explained in section 3. The simulations were done for a very small period of time ($\sim$0.1 μs) in order to avoid the element distortion.

3. Experimental methods

In this section, the experimental methods that were used to obtain mechanical properties are explained in brief. These methods have been explained in detail earlier as well [21, 33, 49]. In order to create samples, AP particles were embedded manually into a HTPB binder. The HTPB binder was created by mixing R-45M liquid polybutadiene and Isophorone Diisocyanate (IPDI) at an index ratio of 1.05. The mixture was then poured into a Teflon mold. The AP particles were embedded with a structured and predetermined amount of spacing, and the samples were cured in a 60 °C oven for 7 days. When fully cured, the sample was carefully cut down to an appropriate diameter and thickness. In order to study the effect of chemical composition, two types of samples were created: sample 1 consisted of HTPB and AP without binding agent and Sample 2 consisted of HTPB, AP and a binding agent Tepanol.

3.1. Constitutive model for HTPB, AP and interface

The constitutive material model and the CZM parameters were obtained from a nanoscale dynamic impact experiment and *in situ* mechanical Raman spectroscopy (MRS) experiment, respectively. The nanoscale dynamic impact experiment used in this work is capable of performing precise impacts at the interfaces. A strain-rate dependent stress-strain law was obtained using a nanoscale dynamic impact experiment [21]. The stress, strain and strain rate data is then fitted to define the material constitutive behavior [21], given by a power law viscoplastic constitutive model

Table 2. Constitutive model parameters for bulk and interface [21].

Parameter		χ (MPa)$^{-n}$	m	n
HTPB		0.54	−0.18	1.8
AP		3.7E10	−9.8	5.9
HTPB-AP interface	Sample 1	1.0E5	−5.0	2.5
	Sample 2	1.0E4	−4.2	2.0

Table 3. Cohesive zone parameters of bulk and interface [21].

Material/interface		Cohesive strength (MPa)	Critical displacement (mm)	Cohesive energy (N mm^{-1})
HTPB		0.8	0.5	0.2
AP		2×10^3	5×10^{-3}	5.0
Interface	Sample 1	1.1	0.12	0.065
	Sample 2	2.91	0.11	0.16

$$\overline{\varepsilon}^{vp} = \chi(\dot{\overline{\varepsilon}}^{vp})^m(\overline{\sigma})^n. \tag{13}$$

Here $\overline{\varepsilon}^{vp}$ is the effective viscoplastic strain and $\overline{\sigma}$ is the equivalent stress. The parameters χ, m and n for the above viscoplastic model is given in table 2 [21].

3.2. CZM for HTPB, AP and interface

In this work, *in situ* MRS tests, as proposed by Prakash *et al* [21], were performed in order to obtain the cohesive zone parameters. The experiments start with an initial crack at the analyzed AP-HTPB interfaces in samples loaded in tensile loading. As load and displacement are applied, the interface crack further extends. The crack extension energy can be calculated based on load displacement relation. The stresses at the crack tip during crack extension are calculated using MRS. The strength of the interface was evaluated from the stress map obtained using MRS by assuming the strength to be equal to the stress at the start of the delamination. A combination of these measurements is used to derive cohesive law parameters. Cohesive zone parameters for bulk HTPB, AP and different interfaces are given in table 3 [21].

3.3. Shock viscosity for HTPB-AP interface

Shock viscosity is the ratio of the maximum stress to the applied strain rate [13]. In order to obtain the shock viscosity, direct measurement of localized stress and strain rate are required. Interface shock viscosity was obtained using a combined pulse laser induce impact experiment and MRS [20]. A pulse laser (1064 nm, 2.5 mJ pulse energy and 9 ns pulse width by Opto-engine LLC) setup is used to accelerate a Si particle that precisely impact HTPB-AP interfaces. The velocity of the impacting particle was calculated using a high-speed streak camera. The MRS setup is used in combination with the pulse laser induced impact setup in order to measure stress *in situ* at the HTPB-AP interfaces. Table 4 lists the value of shock viscosity for HTPB, AP and the HTPB-AP interface used in this work.

Table 4. Shock viscosity of HTPB, AP and the HTPB-AP interface (Sample 1 is without binding agent and Sample 2 is with binding agent tepanol).

	HTPB [50]	AP [2]	Sample 1 [20]	Sample 2 [20]
Viscosity (Pa s)	1.5	30	4.8	6

3.4. Thermal conductivity for HTPB-AP interface

In order to model the thermal behavior of the HTPB-AP energetic material, thermal conductivity values of the individual constituents are needed. For the HTPB and AP phases, thermal conductivity values are readily available in literature [51, 52]. However, there are no available thermal conductivity values for the HTPB-AP interface. In this work, an *in situ* MRS method is used to experimentally measure the thermal conductivity at HTPB-AP interface. The experimental method has been explained elsewhere [53–58]. Here a brief summary is presented.

Perichon *et al* [59] were among the first researchers who developed and explored the relation between Raman peak position and temperature change in order to measure temperature distribution and thermal conductivity measurements using Raman spectroscopy. Since then several researchers have shown this method to be an effective and accurate tool in the temperature distribution measurement as well as the thermal conductivity measurement [53, 55]. In order to measure the temperature distribution around an interface, first a correlation between the changes in Raman shift due to known externally applied temperature needs to be obtained. The experimental setup to obtain the calibration relation between Raman shift and the temperature change is shown in figure 2(a). The sample is mounted on a hot-stage where a temperature detector is attached to one end of the sample and the other end was heated using electric coils. An Ar + laser beam (Modu-Laser Inc., UT) of wavelength 514.8 nm was directed at the sample as the sample was being heated. The backscattered laser beam was collected back by an objective and directed to a spectrometer (Acton SP2500; Princeton Instruments Inc., NJ). A low power laser beam (∼5 mW) was used to measure the Raman shift so that the temperature change due to the laser beam remains less than 1 K [53]. In this work, a correlation between the Raman shift of the CH_2 asymmetric stretching mode (figure 2(b)) and the sample temperature was obtained. The Raman shifts at different temperatures were obtained as plotted in figure 2(c). A linear relationship between the Raman shift and the temperature change from the reference value of the sample was fitted to a linear relation, which is given by

$$\Delta w = C \Delta T, \tag{14}$$

where the value of C is obtained from the slope of the linear correlation curve in figure 2(c), which is equal to $0.121 \, \text{cm}^{-1} \, \text{K}^{-1}$. This calibration constant is then used to calculate the temperature change of the samples by measuring the change in Raman shift values.

4. Results and discussion

4.1. Experimental measurement of thermal conductivity

By measuring the laser energy absorbed by the sample and corresponding temperature increase of the laser spot on the sample, the thermal conductivity of the sample can be derived with a heat transfer model. It has been shown that the isothermal conditions can be assumed
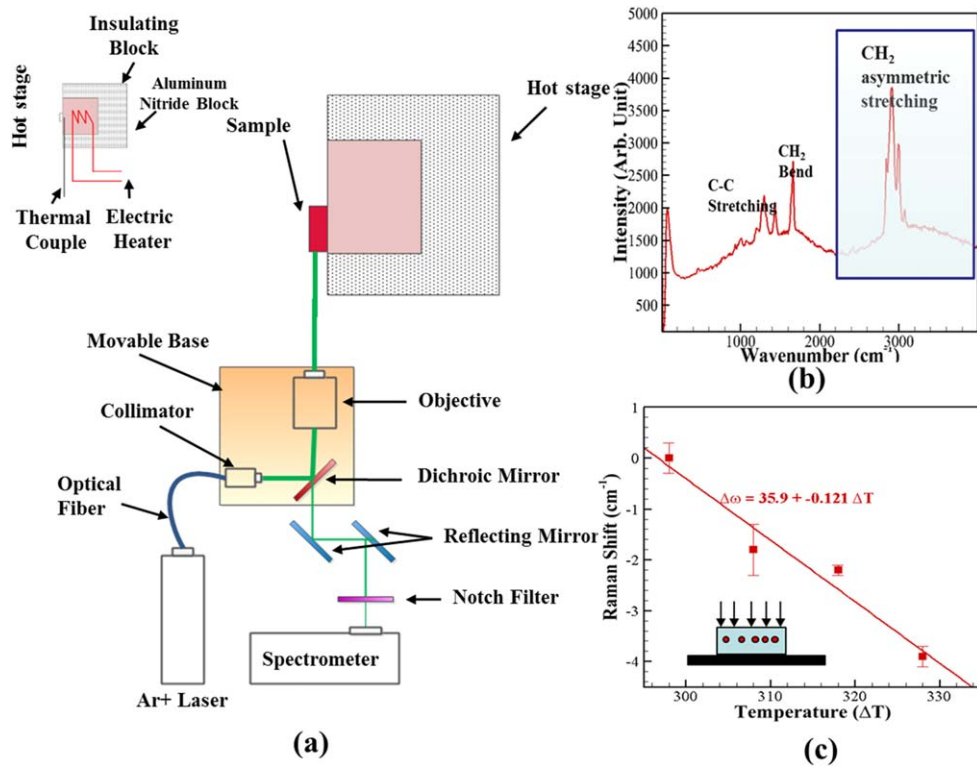
Figure 2. (a) Experimental setup for Raman shift versus temperature change calibration, (b) a representative Raman spectra of HTPB and (c) calibration curve for Raman shift versus temperature change.

and the interface between sample and the substrate can be assumed to be hemispheric, if the thickness of the sample is more than one magnitude larger than the laser spot size [19]. In this work, a 1.2 mm thick HTPB-AP sample was loaded under tensile load. Since the thickness of the sample is much larger (1.2 mm) than the laser spot size ($\sim$1 μm), a linear relation between thermal conductivity and laser power is used as suggested by Nonnenmacher *et al* [60]. A Horiba Xplora Plus Raman spectroscope was used to measure the Raman shift during loading. A 532 nm wavelength laser was used with a laser power of 20 mW and the laser spot size (d) of approximately 1 μm. By measuring the laser power (P) and corresponding temperature change (ΔT) thermal conductivity of the sample can also be calculated using [53]

$$\kappa = \frac{2P}{\pi d \Delta T}. \tag{15}$$

Here, ΔT is the change in temperature of individual scan points, shown in figure 3(b), from the initial bulk temperature [59]. Then, equation (15) directly relates the thermal conductivity to the change in temperature of each individual scan points. In this work, since the laser diameter is $\sim$1 μm, it is assumed that the heat generated by the laser source is responsible for the increase in the local temperature only, which when used in equation (15) results in the local thermal conductivity.
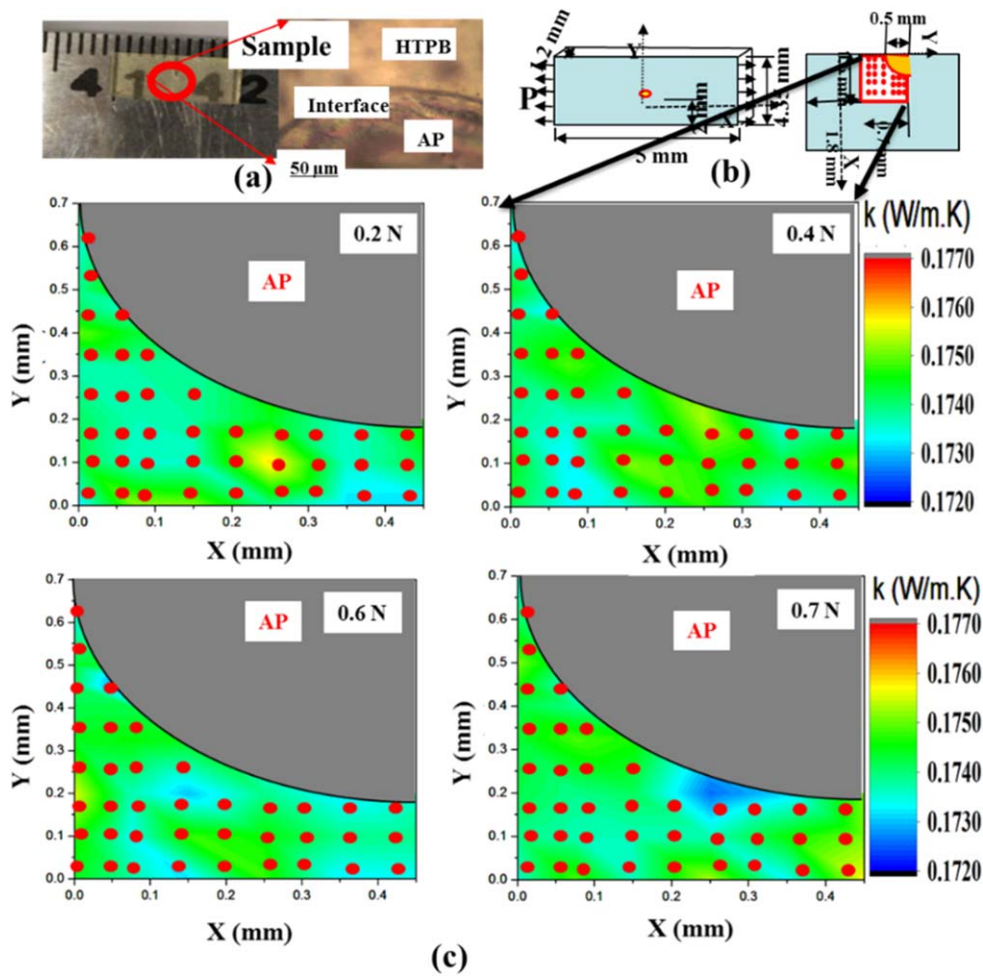
Figure 3. (a) HTPB-AP tensile sample, (b) sample dimensions, boundary conditions and the scan area and (c) thermal conductivity near the HTPB-AP-Tepanol interface. Red dots are the position where Raman spectra were recorded.

Using equation (14) for the temperature change in equation (15), the thermal conductivity can be written as

$$\kappa = \frac{2PC}{\pi d \Delta \omega}.$$

(16)

In this work, a tensile load is applied to a single particle HTPB-AP sample as shown in figure 3(a) and the change in Raman shift near the HTPB-AP interface in the scan area (figure 3(b)) was obtained. Thereafter, equation (16) was used to calculate thermal conductivity of the scan area near the HTPB-AP interface. As can be seen from figure 3(c) for different tensile load, a slight decrease in the thermal conductivity is observed and an average value of 0.175 W m^{-1} K^{-1} was taken to be the interface thermal conductivity for HTPB-AP-Tepanol interface. Similarly, the value of thermal conductivity for HTPB-AP interface, without binding agent, was found to be equal to 0.16 W m^{-1} K^{-1}.

Table 5. Thermal properties of HTPB, AP and the HTPB-AP interface.

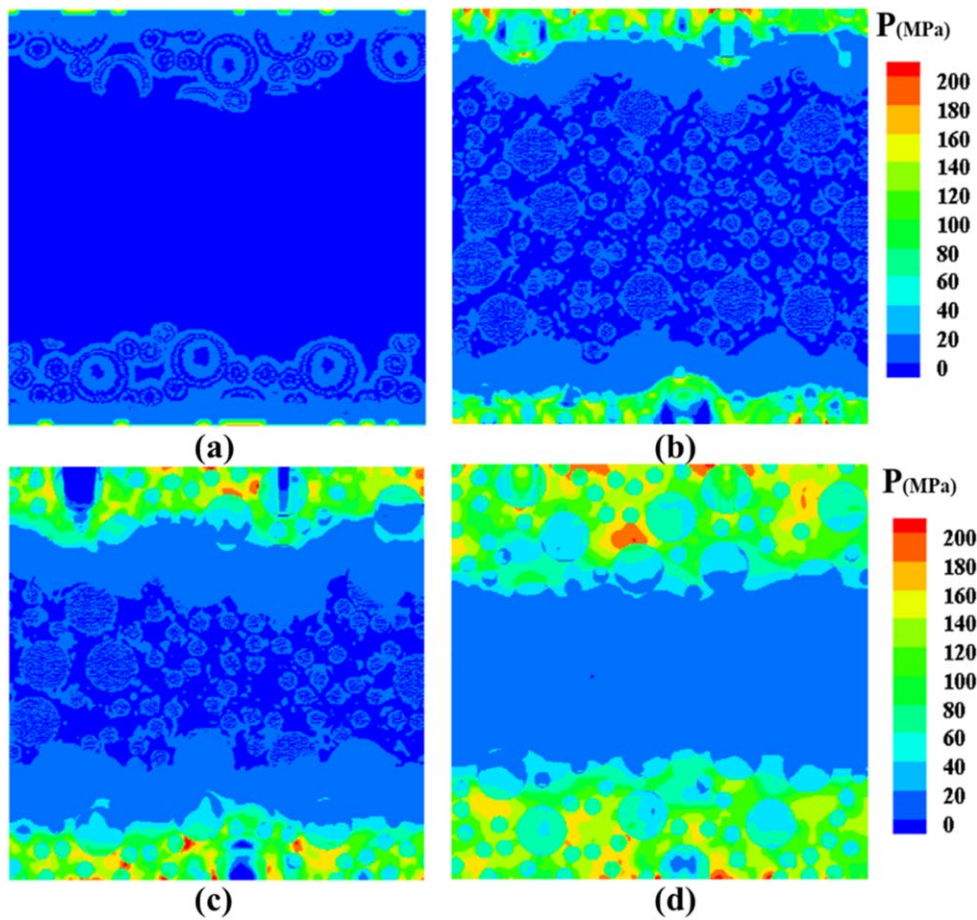|	HTPB	AP	HTPB-AP interface
Thermal conductivity (W m^{-1} K^{-1})	0.28 [62]	0.4 [62]	0.175[20]
Heat capacity (kJ Kg^{-1} K^{-1})	2.5 [52]	1.1 [51]	1.8

4.2. Numerical simulation of shock behavior of HTPB-AP energetic material

The CFEM simulation model described in [20, 21], is used in predicting the effect of interface shock viscosity on the overall microstructure dependent impact behavior and temperature increase due to impact in multi-particle HTPB-AP sample (figure 1). Strain rate dependent power law viscoplastic stress-strain model, as given in table 2, was used for HTPB, AP and the HTPB-AP interface [21]. The CZM parameters, as given in table 3, obtained experimentally through MRS, were used for modeling cohesive separation behavior [49]. The interface shock viscosity is shown in table 4 [20]. Thermal conductivity and heat capacity of the HTPB, AP and the HTPB-AP interface used in the simulation are given in table 5. The value of heat capacity for the HTPB-AP interface was obtained as the average value of AP and HTPB phase values as suggested by Hu *et al* [61]. The models used in this work has been validated in earlier works by the authors [20, 21].

The impact induced local temperature rise in an idealized HTPB-AP EM microstructure (figure 1), with circular AP particles, were simulated. The circular AP particles had radii varying from 5 to 15 μm, [63], with 50% area fraction. In order to understand the effect of individual constituents (HTPB, AP and the HTPB-AP interface) of the microstructure, first the impact behavior of the microstructure was analyzed for a strain rate of 100 000 s^{-1}. The boundary conditions are shown in figure 1. Pressure waves passing through the microstructure are analyzed and the corresponding normal compressive and shear stresses are investigated at different time steps.

Figure 4 shows the pressure wave propagating through the microstructure at different time steps. As shown in figure 4(b), pressure distribution profile near top and bottom surfaces are different, under equal impact velocity of 250 m s^{-1}, due to the difference in the AP particle distribution. As the pressure wave propagates inwards, the interface phase between bulk AP and HTPB phase acts as a barrier and reflects the pressure wave. This creates a lower pressure in larger AP particles as shown in figure 4(c). However, the amount of pressure wave reflection, when propagating from bulk AP phase to HTPB-AP phase is lower than the reflection when propagating from HTPB-AP interface phase to bulk HTPB phase, figure 4(d). This creates a high stress concentration at the HTPB-AP interface phase which leads to deformation and energy localization. The pressure waves are transmitted, without significant reflection, through the interface of HTPB and the AP particles when the particle density is high, i.e. when the amount of bulk HTPB phase separating the particles is small. This can be explained by observing the stress profile along a cross-section with varying AP particle distribution.

The normal compressive stress distribution along a selected cross-section is shown in figure 5. The specific section, figure 5(a), is chosen because of the continuously varying local particle size and density distribution. The position marked A, corresponds to the position at the HTPB-AP interface phase where two particles are separated only by 2 μm which is covered by HTPB-AP interface phase. The position marked B, corresponds to the position inside an AP particle. The position marked C, corresponds to the position inside an AP particle but close to the HTPB-AP interface. As shown in figure 5(b), maximum stress occurs

Figure 4. Pressure map in the HTPB-AP microstructure at time (a) 0.001 μs, (b) 0.002 μs, (c) 0.004 μs and (d) 0.006 μs.

close to the HTPB-AP interfaces around larger AP particles (position A and C). It is observed that initially (at time 0.003 μs) only the interface around large AP particles where particles are closely packed, experiences a higher stress concentration. This is due to the increase in the interaction between AP particles and the stress concentration at the HTPB-AP interfaces as was also reported earlier by authors [20] for a single particle HTPB-AP sample. As time progresses, the normal stress inside the particle (position B) increases but remains below the value at the HTPB-AP interface (position A or C).

In order to understand the mechanism responsible for the maximum stress at the interface, the normal stress distribution near the HTPB-AP interface is plotted. Figure 6 shows a normal stress distribution, where AP particles are close to each other (near position A shown in figure 5), in individual constituents (HTPB, AP and HTPB-AP interface) of the microstructure. It is observed, that the stress wave reflection is insignificant at interfaces where AP particles are separated only by the HTPB-AP interface phase and the stress wave gets transmitted further. This is because the reflection coefficient [64] of HTPB-AP interface phase with the AP phase is low ($R = 0.24$) as compared to that between HTPB and AP phase ($R = 0.98$) or between HTPB and HTPB-AP interface phase ($R = 0.97$).
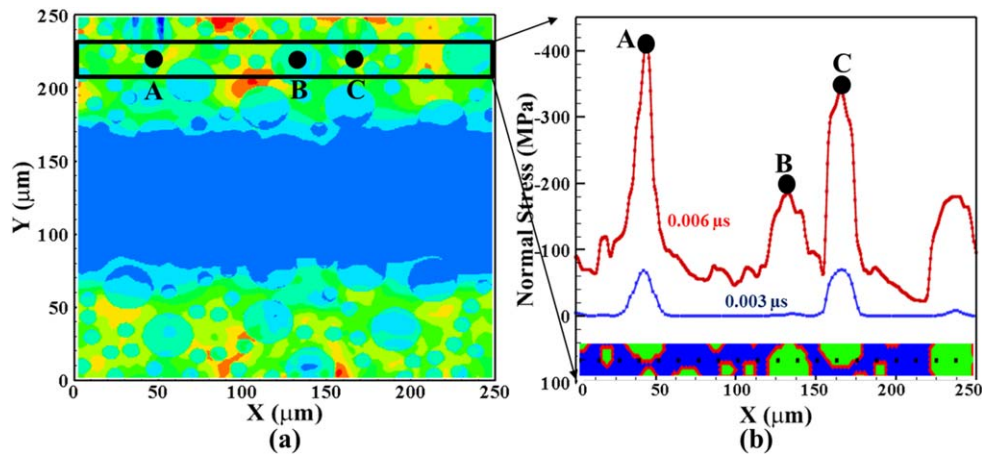
Figure 5. Normal stress profile in the microstructure along a selected cross-section at two different time steps.

Shear stress play a dominant role in determining the interface failure behavior in the material as well as the temperature rise due to frictional heat dissipation [65]. The shear stress distribution in the HTPB-AP microstructure is shown in figure 7. It is observed that the shear stress propagates along the HTPB-AP interface phase only. It can also be seen that the shear stress are highly localized near the HTPB-AP interface and remains concentrated at these positions. This can be further analyzed by studying the shear stress localization in the interface region.

The shear stresses distribution near a HTPB-AP interface region where particles are in close vicinity is shown in figure 8. Shear stress in the bulk HTPB (figure 8(a)) and AP (figure 8(b)) are negligible and are concentrated in the HTPB-AP interface phase only, figure 8(c). This is because the interface boundaries can act as a source, as well as a barrier, to the shear wave [65], depending on where the shear localization starts. In this case, since the localization starts at the interface, as shown in figure 7(a), the shear stress remains concentrated along the interface itself and does not propagate further into the bulk, figures 7(b)–(d). This shear localization behavior then results in an increased viscoplastic and frictional dissipation near the HTPB-AP interface region which leads to a local increase in the temperature.

Internal energy, in equation (10), consists of elastic strain energy and viscoplastic dissipation energy. Viscoplastic dissipation is directly proportional to the magnitude of viscoplastic strain and the stress. The distribution of effective viscoplastic strain within the HTPB-AP microstructure is plotted in figure 9. It is observed that the effective viscoplastic strain in the HTPB-AP interface phase is higher than the AP particles. Similarly, the value of effective viscoplastic strain is higher in the HTPB near the HTPB-AP interface phase where the particle density is high.

Figure 10 shows the temperature increase in the microstructure. Because of the high stress condition at the top boundary, which is under constant compression, a higher value of temperature is reached much earlier than the bulk. However, as the stress wave propagates further into the microstructure, due to the variation in the AP particle distribution, stress and strain inside the microstructure vary significantly which leads to significant variation in energy dissipation. Increase in temperature within the microstructure occurs due the energy dissipation in the form of viscoplastic dissipation and the frictional heat dissipation as evident from equation (9). It is observed from figure 10, that the temperature increase is localized at

13
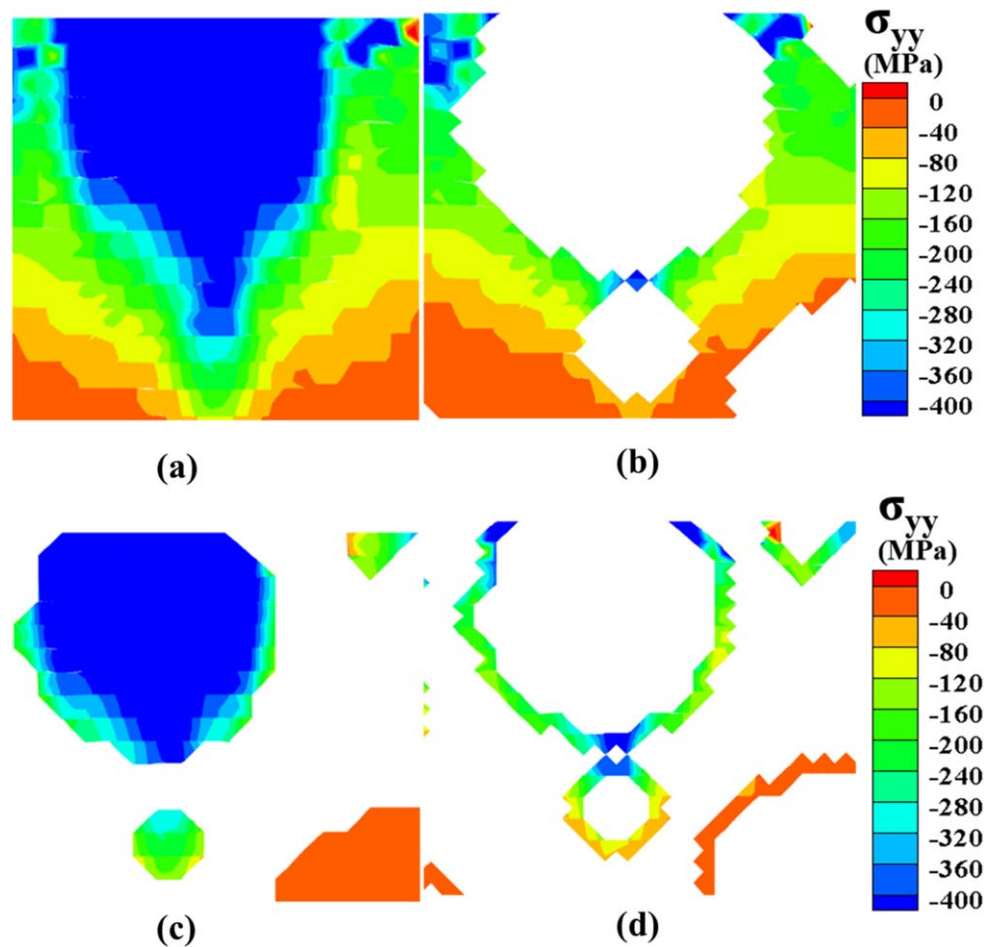
Figure 6. Normal stress distribution in the (a) microstructure at the HTPB-AP interface near position A shown in figure 5, (b) HTPB, (c) AP and (d) the HTPB-AP interface at $t = 0.006 \, \mu s$.

the HTPB-AP interface phase. The temperature localization is greater at positions within the microstructure where particle density is high. This can be explained based on the stress and viscoplastic strain distribution shown earlier. As shown in figures 8 and 9, the shear stress and the viscoplastic strains are maximum in the HTPB-AP interface phase. This contributes to the higher viscoplastic dissipation at the HTPB-AP interface. Also, the normal stresses show a jump in the value near the position of high density AP particles. This stress concentration at the HTPB-AP interface phase, increases the strain energy density in this phase which results in the increase in temperature.

The effect of interface shock viscosity on the impact behavior and the corresponding local temperature change in the HTPB-AP microstructure is studied next. First the deformation behavior and the effect of interface shock viscosity is studied. Figure 11 shows the values plotted for effective normal stress (figure 11(a)) and effective shear stress (figure 11(b)) history in the HTPB-AP microstructure. Effective stress was calculated based on the area average as [2]
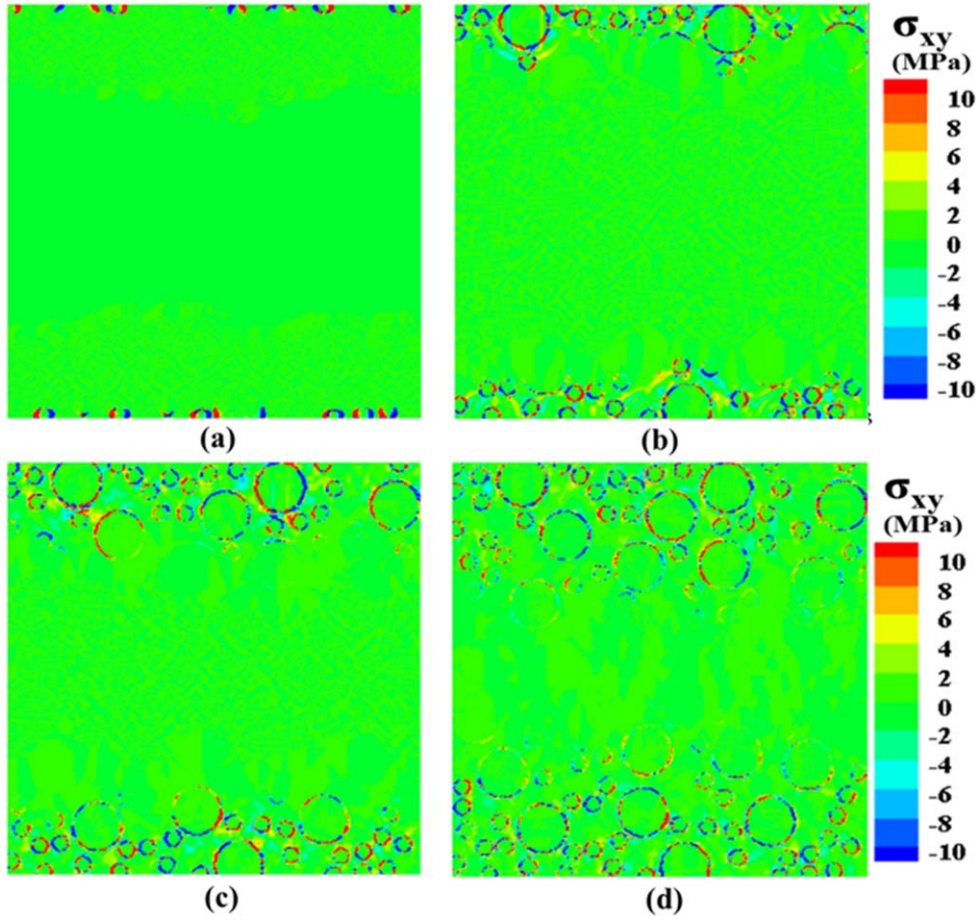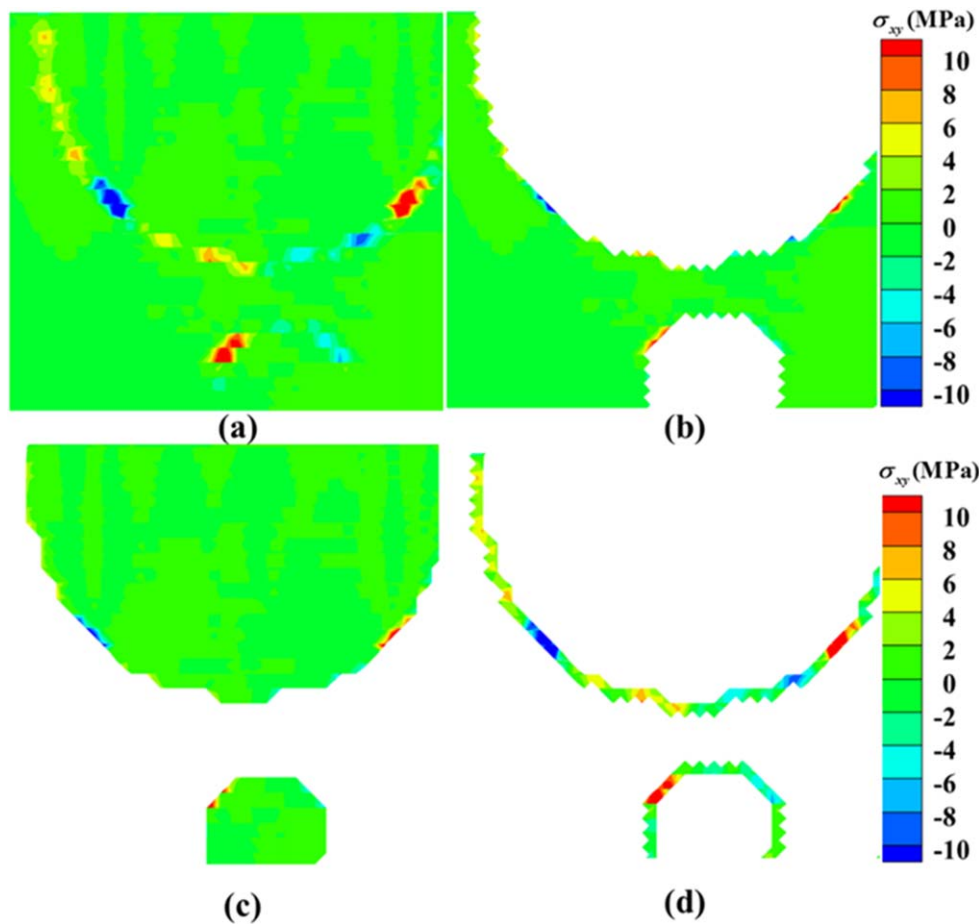
Figure 7. Shear stress distribution in the HTPB-AP microstructure at time (a) 0.001 μs, (b) 0.002 μs, (c) 0.004 μs and (d) 0.006 μs.

$$\sigma_{ij} = \frac{1}{A}\sum_e \sigma_{ij}^e A^e, \tag{17}$$

where σ_{ij}^e and A^e are the elemental stress and area respectively. As shown in figure 11 both the normal and shear stress increases with an increase in the shock viscosity. This is due to the increase in the shock stress within the microstructure that occurs due to increase in viscous effect within the microstructure, especially at the HTPB-AP interface phase. Shear stress shows a more significant effect of interface shock viscosity. This is because the shear stress, as was shown in figure 7, was found to be concentrated only at the HTPB-AP interface whereas all three phases (HTPB, AP and the HTPB-AP interface) show a significant contribution to the effective normal stress. This is illustrated next by plotting the normal and shear stress in all three phases separately, figure 12.

Normal stress and shear stress in HTPB, AP and HTPB-AP interface phases are plotted in figure 12. Normal stress values are significant in all three phases; however, the HTPB-AP interface phase has the highest concentration as was observed in figure 5 as well. Normal stress concentration in the HTPB-AP interface is twice of that in the HTPB phase. Similarly,
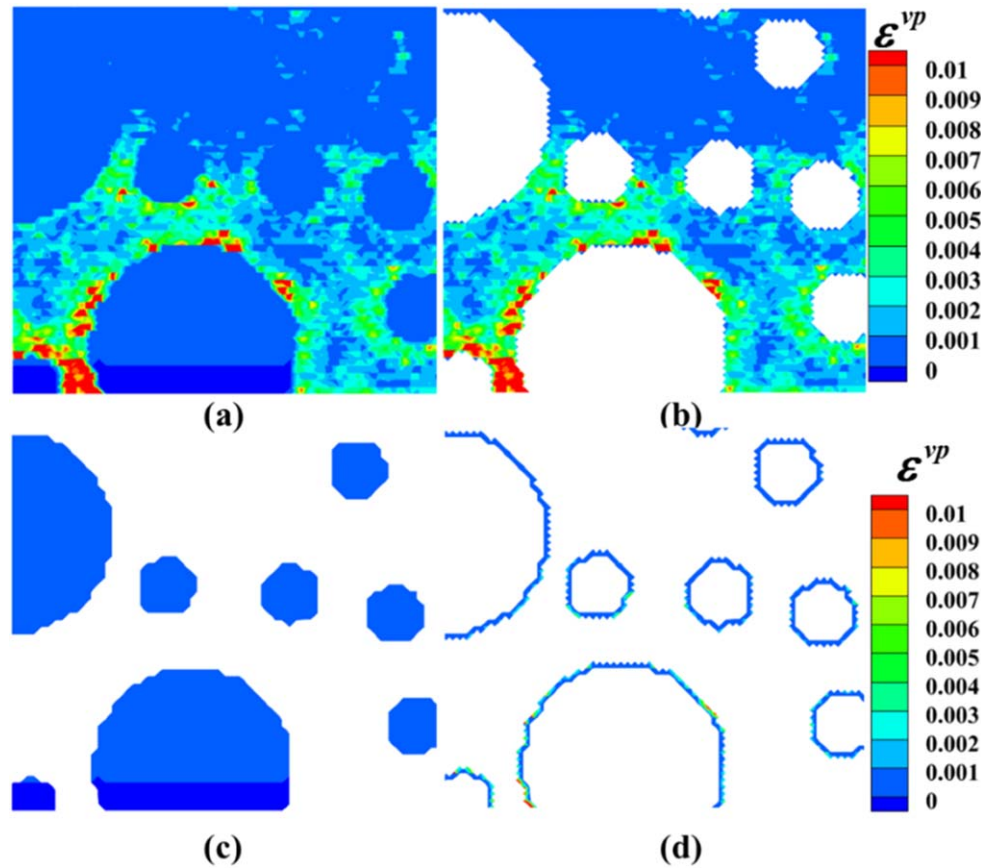
Figure 8. Shear stress distribution in the (a) microstructure at the HTPB-AP interface near position *A* shown in figure 5, (b) HTPB, (c) AP and (d) the HTPB-AP interface at 0.006 μs.

shear stress is concentrated in the HTPB-AP interface phase and the other two HTPB and AP bulk phases have a very low amount of shear stress present. The shear stress value in the HTPB-AP phase is 20 times greater than that in the HTPB phase. This trend was observed in the entire HTPB-AP microstructure, shown in figures 7 and 8 earlier. The interface shock viscosity affects both normal and shear stress and the most significant effect is observed on the shear stress value in the HTPB-AP interface phase. It can also be seen that the normal and shear stresses increases with the increase in interface shock viscosity in the HTPB-AP interface phase, whereas both stresses decrease in the HTPB phase. This is because, as the interface shock viscosity increases, the stress concentration in the HTPB-AP phase increases which results in a decrease in stress in the HTPB phase. Normal stress in the AP phase increases with increasing interface shock viscosity, but the increase is insignificant (~0.5 MPa increase) as compared to HTPB-AP interface phase (~50 MPa).

The effect of interface shock viscosity on the local impact behavior and temperature change in an HTPB-AP microstructure, along a horizontal cross-section, shown in

Figure 9. Effective viscoplastic strain distribution in the (a) microstructure at the HTPB-AP interface near position *A* shown in figure 5, (b) HTPB, (c) AP and (d) the HTPB-AP interface at 0.006 μs.

figure 13(a), is discussed next. This cross-section contains different sizes and density of AP particles, as well as the HTPB and HTPB-AP interfaces. The distribution of normal stress (figure 13(b)), shear stress (figure 13(c)) and temperature (figure 13(c)) as a function of interface shock viscosity is plotted. The variation in the stress profile of both normal and shear shows the stress concentration in the HTPB-AP interface phase. The magnitude of the stress concentration however changes with the interface shock viscosity. The temperature profile, in figure 13(d), shows that the temperature jumps to a higher value in the HTPB-AP interface phase and drops again inside the HTPB and AP phase. Also, as the interface shock viscosity increases, the temperature decreases significantly at the HTPB-AP interface positions where particle density is low. However, near the HTPB-AP interface phase, where the particle interaction is high, the effect of interface shock viscosity is low. This can be observed from figure 13(d), when the temperature profile between position A (higher particle interaction) and position B (low particle interaction) is compared. Position A shows negligible temperature change with interface shock viscosity as compared to position B. Also, as can be observed from figure 13(d), the temperature shows a decrease in the value with increasing interface shock viscosity when transitioning from HTPB to AP phase due to the presence of the
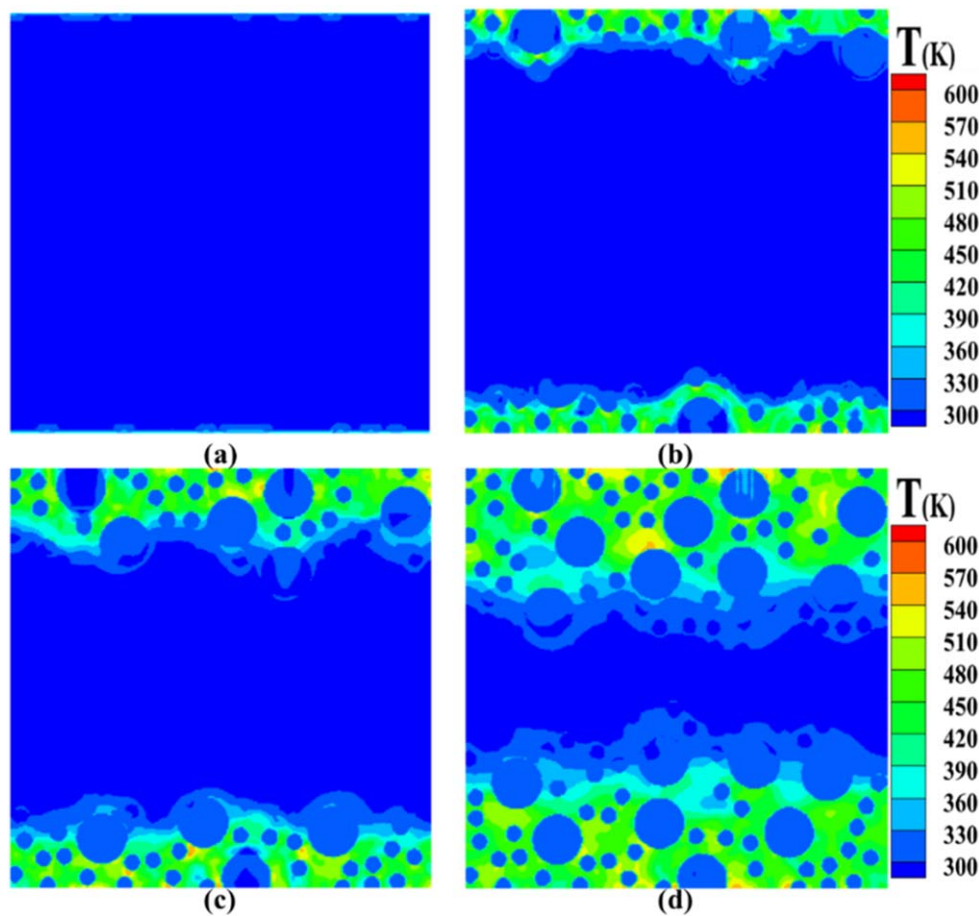
Figure 10. Temperature distribution in the HTPB-AP microstructure at (a) 0.001 μs, (b) 0.002 μs, (c) 0.004 μs and (d) 0.006 μs.

HTPB-AP interface phase. This occurs due to the fact that the energy dissipation at the shock front increases with the interface shock viscosity which leads to a decrease in the temperature.

The temperature change in the microstructure is a function of the plastic and frictional heat dissipation as given in equation (9). The viscoplastic deformation was observed to have a higher value within the HTPB-AP interface phase and the bulk HTPB near the interface than that in the AP, as was shown in figure 9. A plastic dissipation and frictional dissipation energy history as a function of interface shock viscosity is shown in figures 14(a) and (b) respectively. As shown, both energy dissipation decreases with increase in interface viscosity. It has also been discussed earlier [20], that the effect of interface shock viscosity is to widen the interface shock front which leads to a decrease in the dissipation energy and the temperature near the interface.

Impact induced temperature may increase to, or greater than, a certain threshold value, within the microstructure, at several position simultaneously. A measure of such local temperature rise can be taken to be equal to the number of elements per unit area within the HTPB-AP microstructure which rises above a threshold temperature value. In this work, this number density is assumed to be the 'hot-spot' density. The maximum temperature that occurs in the HTPB-AP microstructure and the hot-spot density in the corresponding time
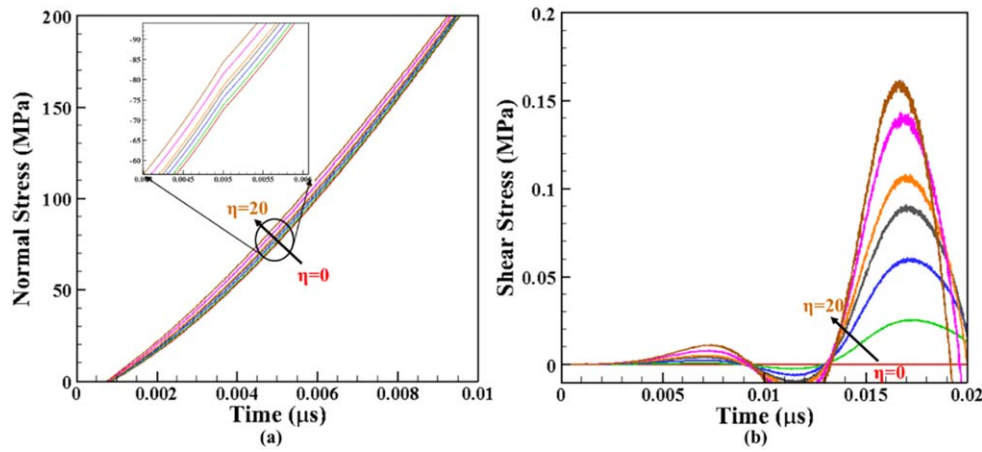
Figure 11. (a) Effective normal compressive stress and (b) effective shear stress history as a function of shock viscosity in the HTPB-AP microstructure.
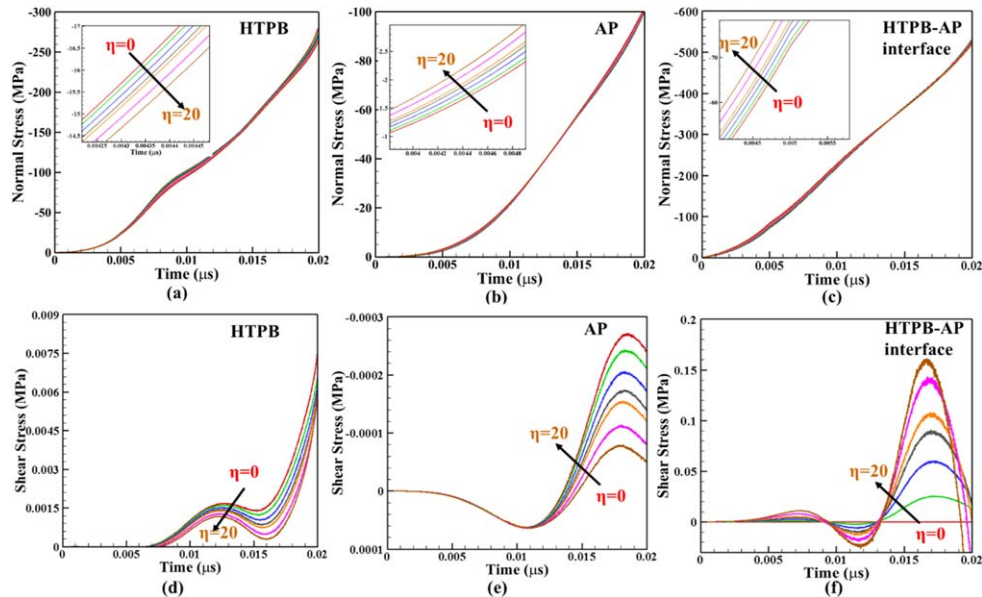
Figure 12. Normal stress (a)–(c) and shear stress (d)–(f) history in HTPB, AP and HTPB-AP interface phase as a function of interface shock viscosity.

interval is shown in figures 15(a) and (b) respectively. A cut-off temperature was selected for hot-spot density calculation based on the decomposition temperature of HTPB and AP. Decomposition of HTPB binder starts at around 673 K whereas at 513 K a phase change occurs in the AP crystals [66]. In this work the maximum temperature for comparison is taken to be 500 K, which is the temperature after which AP phase change starts to occur [66]. It is observed that the maximum temperature, within the microstructure, decreases by more than 20 K by adding interface shock viscosity in the model. This is in agreement with the effect of shock viscosity obtained by Benson [2] in a shocked granular HMX. Correspondingly, the
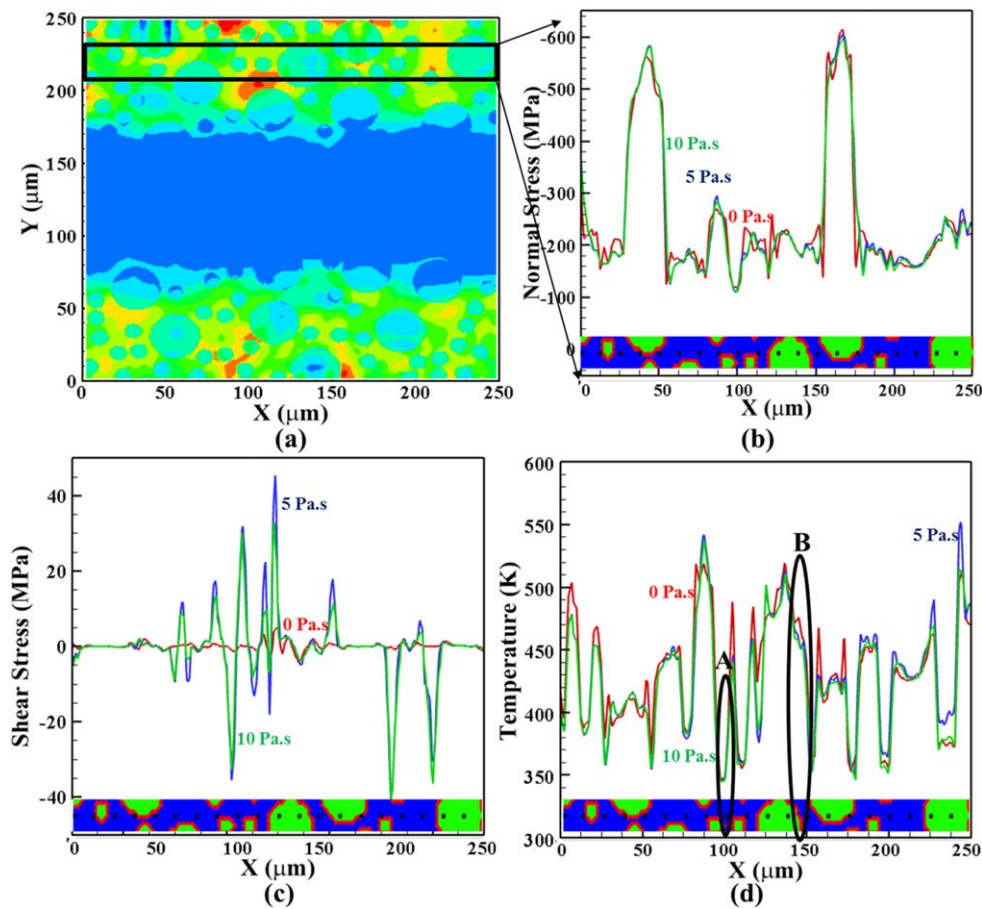
Figure 13. (a) HTPB-AP microstructure, (b) normal stress, (c) shear stress and (d) temperature profile as a function of interface shock viscosity along the selected cross-section at $t = 0.006$ μs.
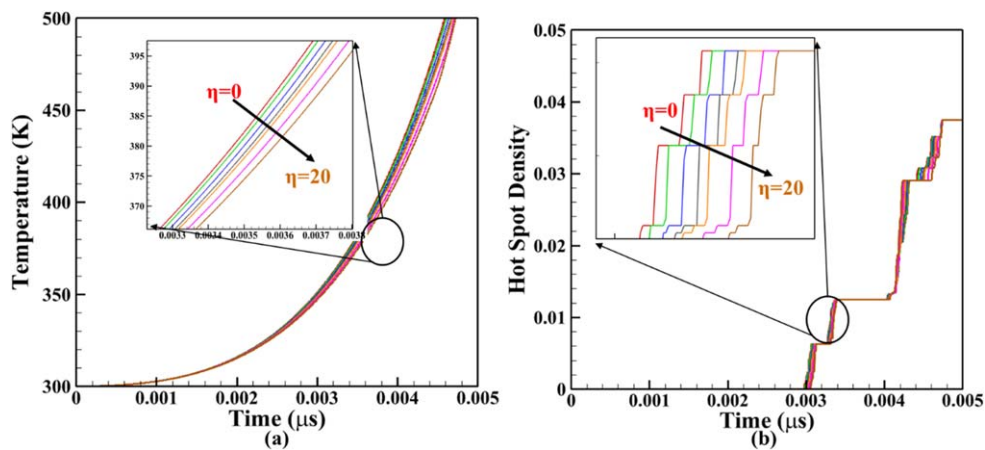
hot-spot density in the microstructure also decreases. Figures 16(a)–(c) shows the plastic dissipation, the maximum temperature in the microstructure and the hot-spot density as a function interface shock viscosity. Figures 16(a)–(c), for comparison purposes, were plotted at the time step, when the maximum temperature, in the case of zero interface shock viscosity, reaches 500 K. It is to be noted that in the current work only 6% area fraction of the microstructure is modeled with HTPB-AP interface phase properties. The stress, dissipation energy and the temperature decrease in the microstructure was found to be significant and in order to predict the temperature increase accurately in EM composites, numerical simulation models should account for the shock viscosity and the effect of interfaces.

5. Conclusions

In this work, the effect of interface shock viscosity on the shock induced deformation and local temperature rise behavior of HTPB-AP EM microstructure were studied. It was shown that the interface shock viscosity plays an important role in determining the local temperature
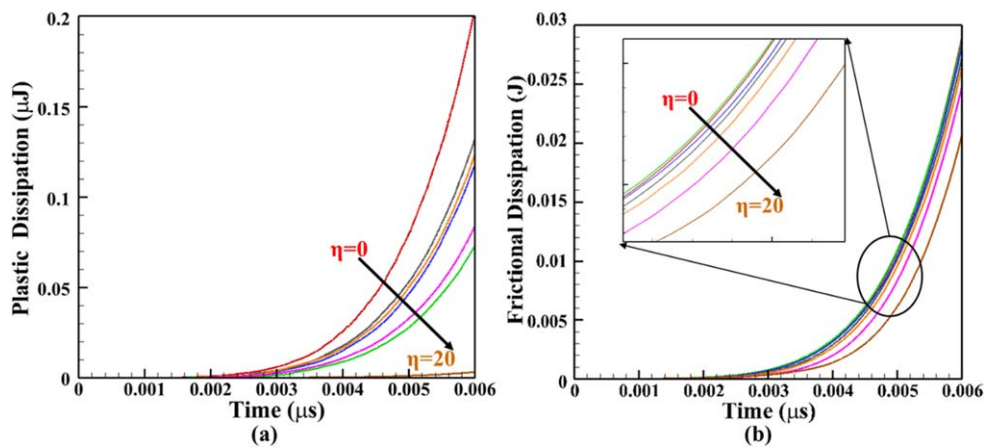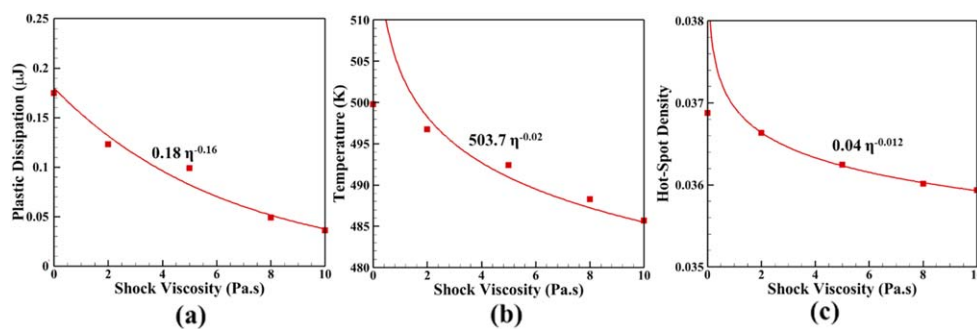
Figure 14. To (a) Viscoplastic and (b) frictional energy dissipation history in the HTPB-AP microstructure as a function of interface shock viscosity.

Figure 15. (a) Maximum temperature in the microstructure and (b) the hot-spot density history as a function of interface shock viscosity.

rise within the microstructure and should be included in the simulation models. Experimentally obtained mechanical properties, such as the strain rate dependent constitutive model, irreversible bilinear cohesive model, interface thermal conductivity and interface shock viscosity were used to model the shock induced deformation behavior using CFEM. Temperature maps showed that the HTPB-AP interfaces, in the energetic material, are the critical positions where the local temperature rise is maximum and are the position where shock initiation may start. Regions with a high density of particles were found to be more susceptible to local temperature rise due to the presence of viscoplastic dissipation, as well as frictional heating. The viscoplastic dissipation were found to be most significant in the HTPB-AP interface phase. The bulk HTPB showed a lower viscoplastic dissipation than the HTPB-AP interface phase but is higher than that in the AP particle. The increase in the interface shock viscosity lead to a decrease in the viscoplastic and frictional dissipation which was caused by the increasing energy dissipation at the shock front. This resulted in a decrease in

Figure 16. (a) Plastic dissipation energy, (b) maximum temperature and (b) the hot-spot density in the HTPB-AP microstructure at $t = 0.005$ μs as a function of interface shock viscosity.

the maximum temperature achievable within the HTPB-AP microstructure. Finally, a power law relation between viscoplastic energy dissipation, temperature rise, and the density of the local temperature rise, as a function of the interface shock viscosity was obtained. The microstructure in this work was idealized as having a 50% AP particles of circular shape having radius from 5 to 15 μm. For a more realistic model of the temperature rise and deformation, a varying shape and density of AP particles needs to be studied.

Acknowledgments

ORCID iDs

Chandra Prakash ⬚ https://orcid.org/0000-0001-9532-4283
Vikas Tomar ⬚ https://orcid.org/0000-0002-2925-7681

References

[1] Field J E, Bourne N K, Palmer S J P and Walley S M 1992 Hot spot ignition mechanism for explosives and propellants *Phil. Trans. R. Soc.* A **339** 269–83
[2] Benson D J and Conley P 1999 Eulerian finite-element simulations of experimentally acquired hmx microstructures *Modelling Simul. Mater. Sci. Eng.* **7** 333–54
[3] Dienes J K 1984 Frictional hotspots and propellant sensitivity *Mater. Res. Soc. Symp. Proc.* **24** 373–81
[4] Bennett J G, Haberman K S, Johnson J N, Asay B W and Henson B F 1998 A constitutive model for the non shock initiation and mechanical response of of high explosives *J. Mech. Phys. Solids* **46** 2303–22
[5] Palmer S J P, Field J E and Huntley J M 1993 Deformation, strengths and strains to failure of polymer bonded explosives *Proc. R. Soc.* A **440** 399–419
[6] Rae P J, Goldrein H T, Palmer S J P, Field J E and Lewis A L 2002 Quasi-static studies of the deformation and failure of β-hmx based polymer bonded explosives *Proc. R. Soc.* A **458** 743–62

[7] Prakash C, Verma D, Exner M, Gunduz E and Tomar V 2016 Strain rate dependent failure of interfaces examined via nanoimpact experiments *Challenges in Mechanics of Time Dependent Materials* vol 2 (Cham: Spinger) pp 93–102

[8] Drodge D R and Proud W G 2009 The effects of particle size and separation on pbx deformation *AIP Conf. Proc.* **1195** 1381–4

[9] Baida H A, Langlade C, Kermouche G and Ambriz R R 2015 Identifying the stress–strain curve of materials by microimpact testing. Application on pure copper, pure iron, and aluminum alloy 6061-t651 *J. Mater. Res.* **30** 2222–30

[10] Zel'dovich Y B and Raizer Y P 1967 *Physics of Shock Waves and High-Temperature Hydrodynamic Phenomena* ed W Hayes (New York: Academic)

[11] Qu T, Verma D, Alucozai M and Tomar V 2015 Influence of interfacial interactions on deformation mechanism and interface viscosity in α-chitin-calcite interfaces *Acta Biomater.* **25** 325–38

[12] Prieto F E and Renero C 1973 Steady shock profile in solids *J. Appl. Phys.* **44** 4013–6

[13] Kanel G I, Savinykh A S, Garkushin G V, Pavlenko A V and Razorenov S V 2017 Shock wave rise time and the viscosity of liquids and solids *Mechanics for Materials and Technologies* vol 46 (Cham: Springer) pp 257–63

[14] Chhabildas L C and Asay J R 1979 Rise-time measurements of shock transitions in aluminum, copper, and steel *J. Appl. Phys.* **50** 2749–56

[15] Swegle J W and Grady D E 1985 Shock viscosity and the prediction of shock wave rise times *J. Appl. Phys.* **58** 692–701

[16] Sheffield S A, Gustavsen R L and Anderson M U 1997 Shock loading of porous high explosives *High-Pressure Shock Compression of Solids iv: Response of Highly Porous Solids to Shock Loading* ed L Davison *et al* (New York: Springer) pp 23–61

[17] Grady D E 2010 Structured shock waves and the fourth-power law *J. Appl. Phys.* **107** 013506

[18] Brown J L *et al* 2008 Dynamic Compaction of Sand *AIP Conference Proceedings* (955) 1363–6

[19] Zhuang S, Ravichandrana G and Grady D E 2003 An experimental investigation of shock wave propagation in periodically layered composites *J. Mech. Phys. Solids* **51** 245–65

[20] Prakash C, Gunduz I E and Tomar V 2019 Simulation guided experimental interface shock viscosity measurement in an energetic material submitted

[21] Prakash C, Gunduz I E, Oskay C and Tomar V 2018 Effect of interface chemistry and strain rate on particle-matrix delamination in an energetic material *Eng. Fract. Mech.* **191** 46–64

[22] Barua A and Zhou M 2011 A lagrangian framework for analyzing microstructural level response of polymer-bonded explosives *Modelling Simul. Mater. Sci. Eng.* **19** 055001

[23] Barua A, Horie Y and Zhou M 2012 Microstructural level response of hmx-estane polymer-bonded explosive under effects of transient stress waves *Proc. R. Soc.* A **468** 3725–44

[24] Tan H 2012 The cohesive law of particle/binder interfaces in solid propellants *Prog. Propulsion Phys.* **2** 59–66

[25] Tan H, Liu C, Huang Y and Geubelle P 2005 The cohesive law for the particle/matrix interfaces in high explosives *J. Mech. Phys. Solids* **53** 1892–917

[26] Barua A, Horie Y and Zhou M 2012 Energy localization in hmx-estane polymer-bonded explosives during impact loading *J. Appl. Phys.* **111** 054902

[27] Barua A, Kim S P, Horie Y and Zhou M 2013 Computational analysis of ignition in heterogeneous energetic materials *Mater. Sci. Forum* **767** 13–21

[28] Koohbor B, Ravindran S and Kidane A 2015 Experimental study of the meso-scale heterogeneous deformation response of polymer composites *Proc. American Society for Composites: 30th Technical Conf.* vol 30, p 1680

[29] Ravindran S and Kidane A 2016 Meso-scale deformation behavior of polymer bonded energetic material under quasi-static compression *Mechanics of Composite and Multi-functional Materials* vol 7 (Cham: Springer) pp 345–50

[30] Ravindran S, Koohbor B and Kidane A 2017 Experimental investigation of compaction wave propagation in cellular polymers *Int. Digital Imaging Correlation Society. Conf. Proc. of the Society for Experimental Mechanics Series* pp 113–5

[31] Ravindran S, Tessema A and Kidane A 2017 Effect of crystal density on dynamic deformation behavior of pbx *Challenges in Mechanics of Time Dependent Materials* vol 2 (Cham: Springer) pp 87–92

[32] Verma D, Prakash C and Tomar V 2017 Interface mechanics and its correlation with plasticity in polycrystalline metals, polymer composites, and natural materials *Proc. Eng.* **173** 1266–74

[33] Prakash C, Olokun A M, Gunduz I E and Tomar V 2019 Interface mechanical properties in energetic materials using nano-scale impact experiment and nano-mechanical Raman spectroscopy *Nano-Energetic Materials* (Singapore: Springer)

[34] Camacho G T and Ortiz M 1996 Computaional modeling of impact damage in brittle materials *Int. J. Solids Struct.* **33** 2899–938

[35] Ortiz M and Pandolfi A 1999 Finite-deformation irreversible cohesive elements for three-dimensional crack-propagation analysis *Int. J. Numer. Methods Eng.* **44** 1267–82

[36] Tomar V 2009 Insights into the effects of tensile and compressive loadings on microstructure dependent fracture of trabecular bone *Eng. Fract. Mech.* **76** 884–97

[37] Dubey D K and Tomar V 2008 Microstructure dependent dynamic fracture analyses of trabecular bone based on nascent bone atomistic simulations *Mech. Res. Commun.* **35** 24–31

[38] Tomar V 2008 Analyses of the role of the second phase sic particles in microstructure dependent fracture resistance variation of sic-si3n4nanocomposites *Modelling Simul. Mater. Sci. Eng.* **16** 035001

[39] Tomar V 2008 Modeling of dynamic fracture and damage in two dimensional trabecular bone microstructures using cohesive finite element method *J. Biomech. Eng.* **130**

[40] Tomar V and Zhou M 2005 Deterministic and stochastic analyses of fracture in a brittle microstructure system *Eng. Failure Mech.* **72** 1920–41

[41] Tan H, Huang Y and Geubelle P 2005 An energy approach to a micromechanics model accounting for nonlinear interface debonding *41st AIAA/ASME/SAE/ASEE Joint Propulsion Conf. & Exhibit*

[42] Prakash C, Gunduz I E and Tomar V 2018 Interface shock viscosity in energetic material using cohesive finite element method *2018 AIAA/ASCE/AHS/ASC Structures, Structural Dynamics, and Materials Conf.* (American Institute of Aeronautics and Astronautics)

[43] Tomar V, Zhai J and Zhou M 2004 Bounds for element size in a variable stiffness cohesive finite element model *Int. J. Numer. Methods Eng.* **61** 1894–920

[44] Dafalias Y F 1987 Issues on the constitutive formulation at large elastoplastic deformations: I. Kinematics *Acta Mech.* **69** 119–38

[45] Boyce M C, Weber G G and Parks D M 1989 On the kinematics of finite strain plasticity *J. Mech. Phys. Solids* **37** 647–65

[46] Thiruppukuzhi S V and Sun C T 2001 Models for the strain-rate-dependent behavior of polymer composites *Compos. Sci. Technol.* **61** 1–12

[47] Reaugh J E and Lee E L 1997 Shock hugoniot behavior of mixed phases with widely varying shock impedances *Topical Conf. on Shock Compression of Condensed Matter of the American Physical Society (Amherest, MA)*

[48] Baek H and Park K 2018 Cohesive frictional-contact model for dynamic fracture simulations under compression *Int. J. Solids Struct.* **144–145** 86–99

[49] Olokun A M, Prakash C, Gunduz I E and Tomar V 2019 Interface chemistry dependent mechanical properties in energetic materials using nano-scale impact experiment *Dyn. Behav. Mater.* **1** 147–52

[50] Florczak B 2014 Viscosity testing of htpb rubber based pre-binders *Cent. Eur. J. Energ. Mater.* **11** 625–37

[51] Baer A D, Keller J A and Ryan N W 1966 Ignition of ammonium perchlorate composite propellants by convectiveheating *AIAA J.* **4** 1358–65

[52] Chaves F R and Góis J C 2016 Research on the specific heat capacity of pbx formulations based on rdx *J. Aerosp. Technol. Manage.* **8** 352–6

[53] Zhang Y, Gan M and Tomar V 2014 Raman thermometry based thermal conductivity measurement of bovine cortical bone as a function of compressive stress *J. Nanotechnol. Eng. Med.* **5** 021003

[54] Gan M and Tomar V 2014 An *in situ* platform for the investigation of Raman shift in micro-scale silicon structures as a function of mechanical stress and temperature increase *Rev. Sci. Instrum.* **85**

[55] Gan M, Samvedi V and Tomar V 2014 Raman spectroscopy-based investigation of thermal conductivity of stressed silicon microcantilevers *J. Thermophys. Heat Transfer* **29** 845–57

[56] Gan M and Tomar V 2014 Surface stress variation as a function of applied compressive stress and temperature in microscale silicon *J. Appl. Phys.* **116** 073502

[57] Prakash C, Lee H, Alucozai M and Tomar V 2016 An analysis of the influence of grain boundary strength on microstructure dependent fracture in polycrystalline tungsten *Int. J. Fract.* **199** 1–20

[58] Verma D, Exner M and Tomar V 2016 An investigation into strain rate dependent constitutive properties of a sandwiched epoxy interface *Mater. Des.* **112** 345–56

[59] Périchon S, Lysenko V, Remaki B, Barbier D and Champagnon B 1999 Measurement of porous silicon thermal conductivity by micro-Raman scattering *J. Appl. Phys.* **86** 4700–2

[60] Nonnenmacher M and Wickramasinghe H K 1992 Scanning probe microscopy of thermal conductivity and subsurface properties *Appl. Phys. Lett.* **61** 168–70

[61] Hu R, Prakash C, Tomar V, Harr M, Gunduz I E and Oskay C 2016 Experimentally-validated mesoscale modeling of the coupled mechanical–thermal response of ap–htpb energetic material under dynamic loading *Int. J. Fract.* **203** 1–22

[62] Zhang J W, Zhi S J and Sun B 2013 Estimation of thermophysical properties of solid propellants based on particle packing model *Sci. China Technol. Sci.* **56** 3055–69

[63] Kubota N and Miyazaki S 1987 Temperature sensitivity of burning rate of ammonium perchlorate propellants *Propellants Explos. Pyrotech.* **12** 183–7

[64] Garbacz A 2010 Stress wave propagation throughout an interface: pcc composites—concrete substrate in repair system *Archit. Civil Eng. Environ.* **3** 35–44

[65] Needleman A and Ortiz M 1991 Effect of boundaries and interfaces on shear-band localization *Int. J. Solids Struct.* **28** 859–77

[66] Zhang L-K and Zheng X-Y 2018 Experimental study on thermal decomposition kinetics of natural ageing ap/htpb base bleed composite propellant *Defence Technol.* **14** 422–5